Influence of chemical composition and crystallographic orientation on the interfacial magnetism in $BiFeO_3/La_{1-x}Sr_xMnO_3$ superlattices

Er-Jia Guo,[1,†] Manuel A. Roldan,[2] Xiahan Sang,[3] Satoshi Okamoto,[4] Timothy Charlton,[1] Haile Ambaye,[1] Ho Nyung Lee,[4] and Michael R. Fitzsimmons[1,5]

[1] *Neutron Scattering Division, Oak Ridge National Laboratory, Oak Ridge, TN 37831, United States*

[2] *Eyring Materials Center, Arizona State University, Tempe AZ 85287, United States*

[3] *Center for Nanophase Materials Sciences, Oak Ridge National Laboratory, Oak Ridge, TN, 37831, United States*

[4] *Materials Science and Technology Division, Oak Ridge National Laboratory, Oak Ridge, TN 37831, United States*

[5] *Department of Physics and Astronomy, University of Tennessee, Knoxville, TN 37996, United States*

† Present address: Beijing National Laboratory for Condensed Matter Physics, Institute of Physics, Chinese Academy of Sciences, Beijing 100190, China, ejguo@iphy.ac.cn

Abstract

The emergence of magnetism unique to the interface between the multiferroic $BiFeO_3$ (BFO) and the ferromagnetic $La_{1-x}Sr_xMnO_3$ (LSMO) offers an opportunity to control magnetism in nanoscale heterostructures with electric fields. In this paper, we investigate the influence of chemical composition and crystallographic orientation on the interfacial magnetism of BFO/LSMO superlattices. Our results reveal that the induced magnetic moment in the BFO layers is proportional to the saturation magnetization of the LSMO layers. For the (100)-BFO/LSMO (x = 0.2) superlattice, the BFO reaches a record high magnetic moment of ~2.8 μ_B/Fe. No interfacial magnetization is observed at (100)-BFO/LSMO interface when LSMO is an antiferromagnet. In contrast to (100)-oriented superlattices, no induced moment is observed in (111)-BFO layers. Our results suggest the interfacial structural reconstruction may not be a sufficient condition for the enhanced net moment in BFO layer. Instead, spin canting induced by interfacial exchange coupling is proposed in the (100)- but not in the (111)-BFO, leading to the large net magnetization at (100)-oriented interface. This work further demonstrates the importance of exchange coupling across heterointerfaces for the spin canting in nominally antiferromagnets, providing a pathway to control the magnetic properties of artificial oxide heterostructures.

Key words: Interfacial magnetization; multiferroic; polarized neutron reflectometry; manganite; oxide heterostructure

This manuscript has been authored by UT-Battelle, LLC under Contract No. DE-AC05-00OR22725 with the U.S. Department of Energy. The United States Government retains and the publisher, by accepting the article for publication, acknowledges that the United States Government retains a non-exclusive, paid-up, irrevocable, world-wide license to publish or reproduce the published form of this manuscript, or allow others to do so, for United States Government purposes. The Department of Energy will provide public access to these results of federally sponsored research in accordance with the DOE Public Access Plan (http://energy.gov/downloads/doe-public-access-plan).

Introduction

Tailoring the magnetic ground states by artificial design of oxide heterointerfaces enable the opportunities to develop high-performance spintronic devices. [1-5] For example, interfaces between two non-ferromagnetic oxides, like $LaNiO_3/CaMnO_3$, [6] $CaRuO_3/CaMnO_3$, [7] and $YBa_2Cu_3O_7/La_{0.67}Ca_{0.33}MnO_3$, [8] exhibit unexpected ferromagnetism. Many mechanisms have been proposed to explain interfacial magnetism in oxide heterostructures, including charge transfer, [9] orbital ordering, [10, 11] octahedral distortion, [12] and atomic reconstruction. [13, 14] Recently, observation of a large net moment (~ 1.8 μ_B/Fe) in multiferroic $BiFeO_3$ (BFO) interfacial layers was reported when BFO was in proximity to a ferromagnetic $La_{0.7}Sr_{0.3}MnO_3$ layer. [15, 16] Coexistence of ferroelectric and large magnetization in the BFO layer offers the possibility to control magnetism and ferroelectricity simultaneously in a heterostructure. [17, 18] This achievement provides a step ahead towards possible applications in electric-field controlled spintronic devices with low energy cost. An outstanding question is how prevalent is the observation of induced magnetization in BFO?

In this paper, we examined the influence of chemical composition in $La_{1-x}Sr_xMnO_3$ (LSMO) on the interfacial properties of (100)-oriented BFO/LSMO superlattices (SLs), where x is the Sr doping level. The temperature and field dependent magnetization of (100)-oriented BFO/LSMO SLs was systematically investigated. We then studied the influence of crystallographic orientation on BFO/LSMO SLs by comparing the (100)- and (111)- oriented SLs. The magnetic response of each layer to the magnetic field and temperature was measured with magnetometry and polarized neutron reflectometry (PNR).

Sample preparation and structural characterizations on BFO/LSMO SLs

The BFO/LSMO SLs and LSMO single layers were fabricated on $SrTiO_3$ (STO) substrates by pulsed laser deposition. Details of the growth condition can be found in our previous work. [16] Both STO (100)- and (111)-oriented substrates were chemically etched with buffered HF and then annealed under flowing oxygen to ensure the atomically flat step-and-terrace surfaces. [19, 20] The Sr doping level (x) in LSMO layers was varied from 1/8 to 0.6, to compare the LSMO layers being from a ferromagnet (FM) to an antiferromagnet (AFM) at the same temperature. [21] The thickness of LSMO single layer sample was 20 unit cells (u.c.). For the (100)-SLs, the thicknesses of LSMO and BFO layers were 20 and 5 u.c., respectively, and the bilayer was stacked for 10 times for making superlattices. We performed scanning transmission electron microscopy (STEM) measurements to check the local structural crystallinity and interface quality. Figure 1(a) shows a low-magnification STEM high-angle annular dark-field (HAADF) image of a representative (100)-SL (x = 0.3). An atomic-resolution STEM-HAADF image of a selected region (marked as a yellow rectangle in Figure 1a) is shown in Figure 1(b). STEM indicates all layers are uniform, continuous, epitaxial with chemically sharp and coherent interfaces. X-ray reflectivity (XRR) measurements were performed on all samples to determine layer thicknesses. As shown in Figure 1(c), the (100)-SLs ($x \geq 0.3$) show the clear thickness fringes and superlattice peaks, indicating well-defined interfaces between the BFO and LSMO layers. The solid lines in Figure 1(c) describe the best fits to the XRR data (open circles) obtained from GenX. [22] The analysis indicates the chemical composition within each BFO or LSMO layer was uniform. The thickness of LSMO and BFO layers are 7.8(5) and 1.9(4) nm, respectively, and the total thickness for SLs is ~ 100 nm. Figure 2(a) shows the X-ray diffraction (XRD) θ–2θ scans of all (100)-SLs. The (100)-SLs ($x \geq 0.3$) exhibit narrow

superlattice peaks with up to eight orders of Kiessig fringes, confirming the epitaxial growth of high-quality superlattices. With increasing x, the central Bragg peaks from the SLs shift to large 2θ angles. This is due to the lattice constant of LSMO reduces with increasing x, [23] resulting in the averaged out-of-plane lattice parameter of BFO/LSMO bilayer decreases. Reciprocal space maps (RSMs) of all SLs indicate that all layers are coherently strained in the plane to STO substrates [Figure 2(b)]. For the SLs ($x \leq 0.2$), the density difference between BFO and LSMO becomes small, thus the X-ray scattering length density (SLD) contrast across the BFO/LSMO interface is insufficient to distinguish between two layers.

Electrical and magnetic measurements on BFO/LSMO SLs

We measured the electrical transport properties of all samples using the van der Pauw method. [24] As we know, the BFO is a ferroelectric insulator, [25-27] thus the electrical conduction of (100)-SLs occurs through the conducting LSMO layers. Comparing the resistivities of LSMO single layers and (100)-SLs allows us to understand the influence of ferroelectric polarization on the mobile charge density of the LSMO layers. As shown in Figure 3(a)-3(e), the LSMO single layers transition from insulating to metallic phases at low temperatures with increasing x. For $x \geq 0.2$, the LSMO single layers undergo an insulator-to-metal transition as temperature decreases. The room-temperature resistivity of LSMO single layers reduces gradually with the increase of hole concentration (x). The resistivities of (100)-SLs are larger than those of the LSMO single layer with the same x. For the (100)-SL ($x = 0.2$), the resistivity increases by five orders of magnitude compared to that of the LSMO ($x = 0.2$) single layer. In this case, the buried ultrathin LSMO ($x = 0.2$) layer is a ferromagnetic insulator (FMI) at low temperatures in proximity to the BFO layers. Increased resistivity of (100)-SLs can be attributed to the depletion of holes in the LSMO layers due to the intrinsic ferroelectric

remnant polarization of the BFO layers. Since the LSMO (x = 0.2) sits on the phase boundary between an insulator and a metal, [21, 23] a small perturbation of hole concentration might lead to a significant change in the conductivity as well as to the insulator-to-metal transition temperature.

The magnetic properties of all samples were characterized by a superconducting quantum interference device (SQUID). The magnetization was normalized to the total thickness of the LSMO single layers and SLs, respectively. Figure 3(f)-3(j) and Figure 4(a)-4(e) show the $M(T)$ curves and low-field $M(H)$ loops of LSMO single layers and (100)-SLs with different x, respectively. For LSMO single layers, the Curie temperature (T_C) of LSMO increases from 205 to 330 K as x increases from 1/8 to 0.3, then T_C decreases to 267 K when x = 0.5. The saturation magnetization (M_S) of LSMO single layer reaches the maximum value when x = 0.2. Further increase or decrease of x in LSMO layers reduces M_S. No magnetization was detected for LSMO (x = 0.6) single layer due to the AFM nature. The Sr doping dependence of T_C and M_S in LSMO single layers is consistent with bulk LSMO. [21, 23]

For the (100)-SLs, T_C reduces significantly compared to T_C of LSMO single layers with the same x, whereas T_C of (100)-SL (x = 0.5) is nearly the same as the LSMO (x = 0.5) single layer. We also find the coercive fields (H_C) of the SLs [except for SL (x = 0.6)] strongly increase compared to the LSMO single layers. The increase of H_C in (100)-SLs implies interfacial coupling between the BFO and LSMO [11, 28] Previously, our work showed that the spin alignment between Fe and Mn is anti-parallel. The magnetization from BFO layers partially cancels the magnetization from LSMO layers, resulting in a *reduction* of the measured magnetization from the BFO/LSMO superlattices. [16] If we apply the same rule for all SLs in the present work, *i. e.* the net moment of 5 u.c.-thick BFO layer cancels a portion of the net

moment of 20 u.c.-thick LSMO layer, we can estimate the induced magnetization in BFO layer for all (100)-SLs. Figure 4(f) shows the induced magnetization in the BFO layers as a function of the saturation magnetization of LSMO layers. The BFO magnetization is antiparallel to the magnetization of LSMO, as illustrated by different signs of the magnetization. The absolute moment of the induced magnetization in BFO layers is correlated with the saturation magnetization of LSMO. The magnitude of BFO moment within the SL (x = 0.2) reaches the highest value of ~ 420 kA/m (~ 2.8 μ_B/Fe) at 10 K. This value is significantly larger than the previously reported BFO moment in (100)-SL (x = 0.3) [15, 16] and is the largest value reported to date. On the contrary, the magnetization in BFO layer is close to zero for the SL (x = 0.6), indicating no induced magnetization in BFO when the LSMO is an antiferromagnet.

Crystallographic orientation effect on the interfacial magnetization of BFO/LSMO SLs

Next, we report on the influence of crystallographic orientation on the interfacial magnetization by comparing the magnetic response from the (100)- and (111)-oriented SLs and (111)-LSMO (x = 0.3) single layer (Figure 5). In contrast to the (100)-SL, the (111)-SL and (111)-LSMO single layer exhibit nearly identical T_C and M_S. H_C of (111)-SL is only ~ 10 Oe larger than H_C of the (111)-LSMO single layer, in sharp contrast to the dramatic increase of H_C (~ 200 Oe) in (100)-SL. This result suggests the interfacial coupling between the BFO and LSMO across the (111) interface is extremely small. Further, no sizable net magnetization is induced in the (111)-BFO layers along the in-plane direction.

To confirm the negligible moment in the (111)-BFO layers, we performed the PNR experiments on the (111)-SL to quantitatively determine the depth profile of magnetization across the (111)-interfaces at different temperatures. [29] The sample was field-cooled and measured with an in-plane magnetic field of 1 T. Figures 6(a) and 6(b) show the specular

reflectivities of the (111)-SL as a function of wave factor transfer q [= $4\pi\sin(\alpha_i)/\lambda$] at 10 and 300 K, respectively, where λ is the wavelength of neutrons and α_i is the incident angle with respect to the sample surface. R^+ and R^- represent the reflectivities from polarized neutron beam, where "+" and "–" indicate the polarization of neutron beam is parallel or antiparallel to the applied magnetic field, respectively. PNR and XRR data were fitted using GenX. [22] Solid lines are the best fits to the PNR data (open circles) using a structural model derived from the XRR fitting. To illustrate the confidence of our data fitting, we have calculated the spin asymmetries SA [= $(R^+-R^-)/(R^++R^-)$] from the experimental data and fits, as shown in insets of Figure 6(a) and 6(b). The nuclear SLD profile of a (111)-SL indicates the BFO has a higher atomic density than that of LSMO [Figure 6(c)]. We also obtained the magnetic SLD profile, from which we obtain the net magnetization distribution in the sample plane across the interfaces of the (111)-SL. M_{LSMO} is 537(8) kA/m [3.58(5) μ_B/Mn] at 10 K and decreases to 277(5) kA/m [1.85(4) μ_B/Mn] at 300 K. T_C of LSMO in (111)-SL is around 350 K, which is comparable to T_C of a (111)-LSMO single layer. In contrast to the (100)-SL case, [16] M_{BFO} in the (111)-SL is very small with +40(15) kA/m [0.25(10) μ_B/Fe] at 10 K, and slightly drops to +24(15) kA/m [0.15(10) μ_B/Fe] at 300 K. M_{BFO} is parallel to the LSMO magnetization, i. e., the M_{BFO} and M_{LSMO} have the same sign. The PNR results show the induced moment in the BFO layer within (111)-SLs is indeed negligible small compared to that within (100)-SLs.

The origin of large uncompensated net moment in BFO layers with (100) orientation when in proximity to a ferromagnetic LSMO is still debated. Previously, using STEM and XAS, we concluded that charge transfer and chemical intermixing do not contribute to the induced magnetization in BFO layers. [16] Direct observations of the (100)-oriented BFO/LSMO interface by STEM indicate the interfacial BFO layers exhibit structural distortion with a

suppression of octahedral rotation at the interface at room temperature. [30, 31] Such result suggests the structural reconstruction might be a possible mechanism for the induced magnetization in BFO layers. However, the bulk lattice structure of LSMO preserves the rhombohedral phase independent of x. [32] Thus, the possible structural distortion in the interfacial BFO layers in proximity to LSMO(x) will persist for all (100)-SLs. Yet, if true, the consistency of interface structure distortion with x cannot explain the dependence of M_{BFO} with different x as well as different magnetization transition temperatures.

Results and discussions

We suggest an alternate mechanism to explain the chemical composition and crystallographic dependence of M_{BFO}. Canting of Fe spins in the (100)-BFO is due to the interfacial exchange coupling with Mn spins in (100)-LSMO. Bulk BFO has a G-type AFM order with the Fe spins ferromagnetically coupled within the pseudocubic (111) planes but AFM coupled between adjacent planes [Figure 5(c)]. [27] In the (100)-SLs, the exchange coupling at the BFO and LSMO interfaces will cause Fe spins to tilt away from the diagonal towards the direction parallel to the Mn spins, *i. e.* the BFO/LSMO interface, by applying an in-plane magnetic field. [11] The spin canting in BFO produces the in-plane net magnetization at the interface [Figure 5(d)]. The interfacial magnetic coupling is determined by $\boldsymbol{J}_{\text{Fe-Mn}}[\,\vec{\boldsymbol{S}}_{\boldsymbol{Fe}} \cdot \vec{\boldsymbol{S}}_{\boldsymbol{Mn}}]$, [33, 34] where $\boldsymbol{J}_{\text{Fe-Mn}}$ is the exchange coupling constant between Fe and Mn spins, $\vec{\boldsymbol{S}}_{\boldsymbol{Fe}}$ and $\vec{\boldsymbol{S}}_{\boldsymbol{Mn}}$ are the interface spin vectors for the Fe and Mn ions, respectively. $\boldsymbol{J}_{\text{Fe-Mn}}$ and $\vec{\boldsymbol{S}}_{\boldsymbol{Mn}}$ depend on the hole concentration (valence state of Mn ions) in LSMO. [34] Since the effective magnetic field acting to cant the interfacial Fe spins is proportional to $\boldsymbol{J}_{\text{Fe-Mn}}\langle\vec{\boldsymbol{S}}_{\boldsymbol{Mn}}\rangle$, [34] we would expect the stronger saturation magnetization in the LSMO layers, the higher strength of exchange coupling and the larger magnitude of the canting angle between the neighboring spins in BFO, leading to

the larger in-plane magnetization in BFO layers. On the other hand, in the (111)-SLs, the spin moments in BFO align parallel in each {111} plane and the spins in the adjacent planes keep AFM alignment in the plane [Figure 5(e)]. Upon the applied magnetic field, the Fe spins will cant within the plane due to the Dyzaloshinskii–Moriya interaction (DMI), not towards the interface, thus a small net moment in the (111)-BFO layer is produced along the field direction. This situation is the same as the bulk BFO. [27] The magnetic moment in BFO is parallel to the applied field, *i. e.* along with the Mn spin direction. Canting induced by interfacial exchange coupling consistently explains the influence of the saturation magnetization of LSMO and crystallographic orientation on the net magnetization of BFO layers in the BFO/LSMO SLs.

Summary and outlook

In summary, we investigate the influence of chemical composition and crystallographic orientation on the interfacial magnetization of BFO/LSMO(x) SLs. We found that, in the (100)-SLs, the magnitude of the induced net magnetic moment in BFO layer increases monotonically with increasing saturation magnetization of LSMO, which depends upon x. The net magnetization in BFO layers is negligibly small in the (111)-SLs. Canting of Fe spins in BFO induced by the interfacial exchange coupling between Fe and Mn spins could explain all our observations. In the (100)-orientation, a large spin canting towards the interface can be derived from a large saturation moment of LSMO, resulting in an induced large net magnetization in BFO layers; whereas the spins from the adjacent {111} planes in BFO only cant within the plane due to the DMI, thus the negligible net magnetization in (111)-BFO layer is observed. This work demonstrates the importance of spin canting at the oxide interfaces for promoting the exotic magnetic states and suggests a pathway to enhance the net magnetization in nominally AFM materials through modulation of electron correlations. Discovery of large net magnetization with

controllable magnitude in the multiferroic BFO may allow the electric field control of magnetism and enable the energy-efficient spintronic devices.

Acknowledgements

This work was supported by the U.S. Department of Energy (DOE), Office of Science (OS), Basic Energy Sciences (BES), Materials Sciences and Engineering Division (sample design, fabrication, and physical property characterizations). The research at ORNL's Spallation Neutron Source was sponsored by the Scientific User Facilities Division, BES, U.S. DOE.

References

[1] R. Ramesh, and D. Schlom, "*Whither oxide electronics?*" MRS Bull. **33**, 1006 (2008).

[2] N. A. Spaldin, S.-W. Cheong, and R. Ramesh, "*Multiferroics: Past, present, and future*," Physics Today **63**, 38 (2010).

[3] H. Y. Hwang, Y. Iwasa, M. Kawasaki, B. Keimer, N. Nagaosa, and Y. Tokura, "*Emergent phenomena at oxide interfaces*," Nat. Mater. **11**, 103 (2012).

[4] A. Bhattacharya, and S. J. May, "*Magnetic oxide heterostructures*," Annu. Rev. Mater. Res. **44**, 65 (2014).

[5] Frances Hellman, *et al.*, "*Interface-induced phenomena in magnetism*," Rev. Mod. Phys. **89**, 025006 (2017).

[6] A. J. Grutter, H. Yang, B. J. Kirby, M. R. Fitzsimmons, J. A. Aguiar, N. D. Browning, C. A. Jenkins, E. Arenholz, V. V. Mehta, U. S. Alaan, and Y. Suzuki, "*Interfacial Ferromagnetism in $LaNiO_3/CaMnO_3$ Superlattices*," Phys. Rev. Lett. **111**, 087202 (2013).

[7] C. He, A. J. Grutter, M. Gu, N. D. Browning, Y. Takamura, B. J. Kirby, J. A. Borchers, J. W. Kim, M. R. Fitzsimmons, X. Zhai, V. V. Mehta, F. J. Wong, and Y. Suzuki, "*Interfacial Ferromagnetism and Exchange Bias in $CaRuO_3/CaMnO_3$ Superlattices*", Phys. Rev. Lett. **109**, 197202 (2012).

[8] J. Chakhalian, J. W. Freeland, G. Srajer, J. Strempfer, G. Khaliullin, J. C. Cezar, T. Charlton, R. Dalgliesh, C. Bernhard, G. Cristiani, H.-U. Habermeier, and B. Keimer, "*Magnetism at the interface between ferromagnetic and superconducting oxides*", Nat. Phys. **2**, 244. (2006).

[9] J. Hoffman, I. C. Tung, B. B. Nelson-Cheeseman, M. Liu, J. W. Freeland, and A. Bhattacharya, 2013, "*Charge transfer and interfacial magnetism in $LaNiO_3/LaMnO_3$ superlattices*", Phys. Rev. B **88**, 144411. (2013).

[10] J. Chakhalian, J. W. Freeland, H.-U. Habermeier, G. Cristiani, G. Khaliullin, M. van Veenendaal, and B. Keimer, "*Orbital reconstruction and covalent bonding at an oxide interface*," Science **318**, 1114. (2007).

[11] P. Yu, J. S. Lee, S. Okamoto, M. D. Rossell, M. Huijben, C. H. Yang, Q. He, J. X. Zhang, S. Y. Yang, M. J. Lee, Q. M. Ramasse, R. Erni, Y. H. Chu, D. A. Arena, C. C. Kao, L. W. Martin and R. Ramesh, "*Interface ferromagnetism and orbital reconstruction in $BiFeO_3$-$La_{0.7}Sr_{0.3}MnO_3$ heterostructures*", Phys. Rev. Lett. **105**, 027201 (2010).

[12] E. J. Moon, P. V. Balachandran, B. J. Kirby, D. J. Keavney, R. J. Sichel-Tissot, C. M. Schlepütz, E. Karapetrova, X. M. Cheng, J. M. Rondinelli, and S. J. May, "*Effect of Interfacial Octahedral Behavior in Ultrathin Manganite Films*", Nano Letters **14 (5)**, 2509-2514 (2014).

[13] I. Hallsteinsen, M. Moreau, A. Grutter, M. Nord, P.-E. Vullum, D. A. Gilbert, T. Bolstad, J. K. Grepstad, R. Holmestad, S. M. Selbach, A. T. N'Diaye, B. J. Kirby, E. Arenholz, and T. Tybell, "*Concurrent magnetic and structural reconstructions at the interface of (111)-oriented $La_{0.7}Sr_{0.3}MnO_3/LaFeO_3$*", Phys. Rev. B **94**, 201115(R) (2016).

[14] Y. -M. Kim, A. Morozovska, E. Eliseev, M. P. Oxley, R. Mishra, S. M. Selbach, T. Grande, S. T. Pantelides, S. V. Kalinin, and A. Y. Borisevich, "*Direct observation of ferroelectric field effect and vacancy-controlled screening at the $BiFeO_3/La_xSr_{1-x}MnO_3$ interface*", Nat. Mater. **13**, 1019–1025 (2014).

[15] S. Singh, J. T. Haraldsen, J. Xiong, E. M. Choi, P. Lu, D. Yi, X.-D. Wen, J. Liu, H. Wang, Z. Bi, P. Yu, M. R. Fitzsimmons, J. L. MacManus-Driscoll, R. Ramesh, A. V. Balatsky, Jian-Xin Zhu, and Q. X. Jia, "*Induced Magnetization in $BiFeO_3/La_xSr_{1-x}MnO_3$ Superlattices*", Phys. Rev. Lett. **113**, 047204 (2014).

[16] E. J. Guo, J. R Petrie, M. A Roldan, Q. Li, R. D. Desautels, T. Charlton, A. Herklotz, J. Nichols, J. van Lierop, J. W Freeland, S. V Kalinin, H. N. Lee, and M. R Fitzsimmons, "*Spatially Resolved Large Magnetization in Ultrathin $BiFeO_3$*", Adv. Mater. **29**, 1700790 (2017).

[17] Nicola A. Spaldin and Manfred Fiebig, "*The Renaissance of Magnetoelectric Multiferroics*", Science **309**, 39 (2005)

[18] W. Eerenstein, N. D. Mathur, and J. F. Scott, "*Multiferroic and magnetoelectric materials*", Nature **442**, 759 (2005).

[19] T. Ohnishi, K. Shibuya, and M. Lippmaa, D. Kobayashi, H. Kumigashira, and M. Oshima, H. Koinuma, "*Preparation of thermally stable TiO_2-terminated $SrTiO_3$(100) substrate surfaces*", Appl. Phys. Lett. **85**, 272 (2004).

[20] J. Chang, Y. -S. Park, and S. -K. Kim, "*Atomically flat single-terminated $SrTiO_3$ (111) surface*", Appl. Phys. Lett. **92**, 152910 (2008).

[21] Y. Tokura, *Colossal Magnetoresistive Oxides* (Gordon and Breach, London, 1999).

[22] M. Björck and G. Andersson, "*GenX: an extensible X-ray reflectivity refinement program utilizing differential evolution*", J. Appl. Cryst., **40**, 1174-1178 (2007).

[23] John B. Goodenough, "Theory of the Role of Covalence in the Perovskite-Type Manganites [La, M(II)]MnO_3", Phys. Rev. **100**, 564 (1955).

[24] L. J. Van der Pauw, "*A method of measuring specific resistivity and Hall effect of discs of arbitrary shape*", Philips Research Reports **13**, 1–9 (1958).

[25] J. Wang, J. B. Neaton, H. Zheng, V. Nagarajan, S. B. Ogale, B. Liu, D. Viehland, V. Vaithyanathan, D. G. Schlom, U. V. Waghmare, N. A. Spaldin, K. M. Rabe, M. Wuttig, R. Ramesh, "*Epitaxial $BiFeO_3$ Multiferroic Thin Film Heterostructures*", Science **299**, 1719 (2003).

[26] W. Eerenstein, F. D. Morrison, J. Dho, M. G. Blamire, J. F. Scott, N. D. Mathur, "*Comment on "Epitaxial $BiFeO_3$ Multiferroic Thin Film Heterostructures"*", Science **307**, 5713 (2005).

[27] C. Ederer and N. A. Spaldin, "*Weak ferromagnetism and magnetoelectric coupling in bismuth ferrite*", Phys. Rev. B **71**, 060401(R) (2005).

[28] Di Yi, Jian Liu, Satoshi Okamoto, Suresha Jagannatha, Yi-Chun Chen, Pu Yu, Ying-Hao Chu, Elke Arenholz, and R. Ramesh, "*Tuning the Competition between Ferromagnetism and Antiferromagnetism in a Half-Doped Manganite through Magnetoelectric Coupling*", Phys. Rev. Lett. **111**, 127601 (2013).

[29] M. R. Fitzsimmons, S. D. Bader, J. A. Borchers, , G. P. Felcher, J. K. Furdyna; A. Hoffmann, J. B. Kortright, I. K. Schuller, T. C. Schulthess, S. K. Sinha, M. F. Toney, D. Weller, S. Wolf, "*Neutron scattering studies of nanomagnetism and artificially structured materials*", J. Magn. Magn. Mater., **271,** 103-146 (2004).

[30] A. Y. Borisevich, H. J. Chang, M. Huijben, M. P. Oxley, S. Okamoto, M. K. Niranjan, J. D. Burton, E. Y. Tsymbal, Y. H. Chu, P. Yu, R. Ramesh, S.V. Kalinin, and S. J. Pennycook, "*Suppression of Octahedral Tilts and Associated Changes in Electronic Properties at Epitaxial Oxide Heterostructure Interfaces*", Phys. Rev. Lett. **105**, 087204 (2010).

[31] Young‐Min Kim Amit Kumar Alison Hatt Anna N. Morozovska Alexander Tselev Michael D. Biegalski Ilya Ivanov Eugene A. Eliseev Stephen J. Pennycook James M. Rondinelli Sergei V. Kalinin Albina Y. Borisevich, "Interplay of Octahedral Tilts and Polar Order in $BiFeO_3$ Films", Adv. Mater. **25**, 2497–2504 (2013).

[32] J. B. Goodenough, *Magnetism and the Chemical Bond* (Interscience Publishers, New York, pp. 5–17, 1966).

[33] Y. Tokura, N. Nagaosa, "*Orbital Physics in Transition-Metal Oxides*", Science **288**, 462-468 (2000).

[34] S. Okamoto, "*Magnetic interaction at an interface between manganite and other transition-metal oxides*", Phys. Rev. B **82**, 024427 (2010).

Figure and figure captions

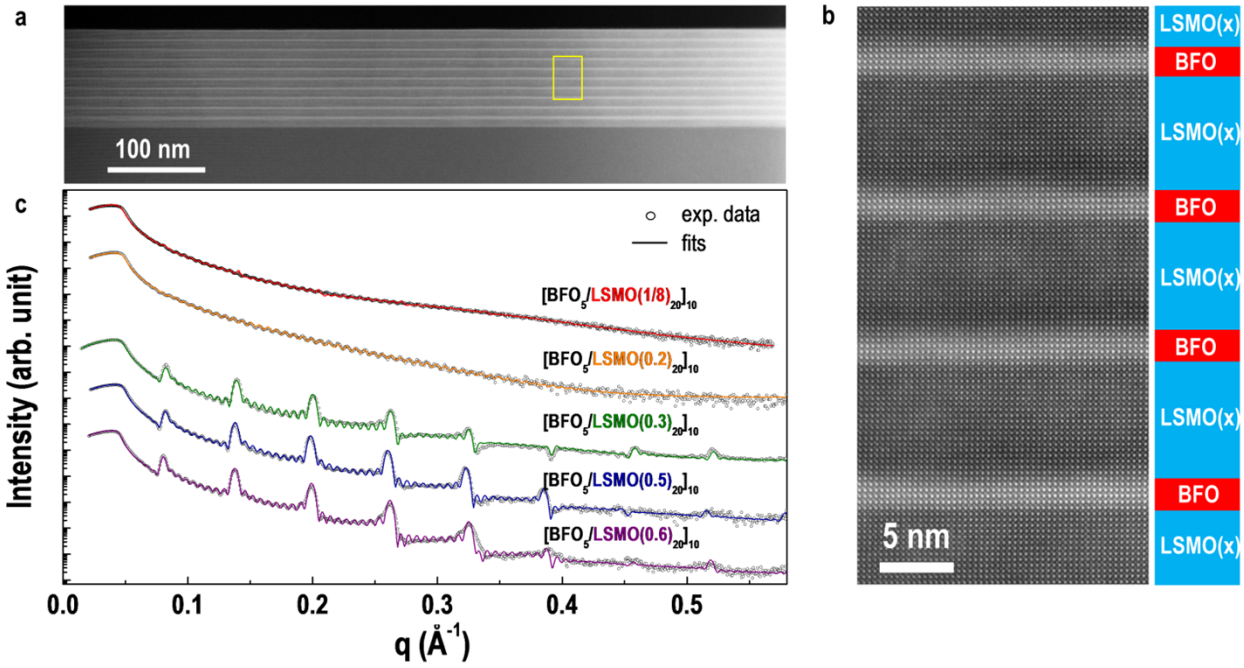

Figure 1. Scanning transmission electron microscopy (STEM) and X-ray reflectivity (XRR) measurements on the BFO/LSMO superlattices (SLs). **a**. Low-magnification STEM- high-angle annular dark-field (HAADF) image of a (100)-SL (x = 0.3), in which the BFO layer thickness is 5 u.c., LSMO layer thickness is 20 u.c., and BFO/LSMO bilayer repeats 10 times. The brightness of layer is proportional to the atomic number Z of the elements. **b**. Atomic-resolution STEM-HAADF image of the same sample in the region, marked with yellow rectangle in **a**. Schematic of the (100)-BFO/LSMO(x) SLs is shown on the right hand of STEM-HAADF image, where x is the Sr doping level. **c**. XRR curves of (100)-SLs with various x. Open circles are the experimental data and the solid lines are the best fits to the XRR data. Using GenX, the chemical depth profiles of (100)-SLs can be determined accurately (not shown). The total thickness of all (100)-SLs is ~ 100 nm. XRR results are in agreement with STEM measurements.

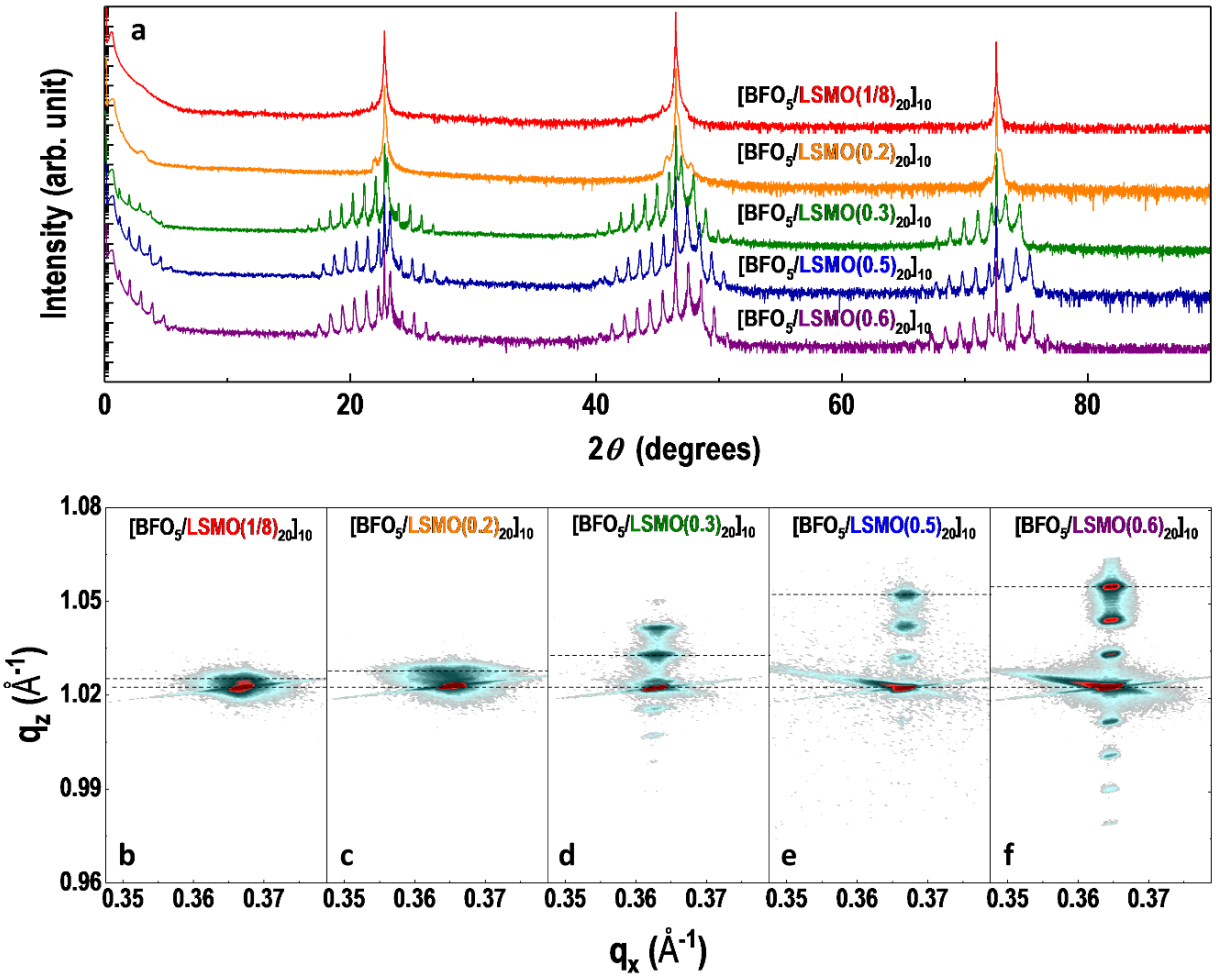

Figure 2. Structural characterization of the BFO/LSMO SLs. **a**. X-ray diffraction (XRD) θ–2θ scans of (100)-SLs with various x. For the (100)-SLs ($x \geq 0.3$), the superlattice peaks up to eight orders of Kiessig fringes were observed, indicating the epitaxial growth of high-quality superlattice. For the (100)-SLs ($x < 0.3$), the superlattice peak was not obvious due to the low density contrast between the BFO and LSMO. **b** to **f**. Reciprocal space maps (RSMs) of (100)-SLs around the substrate's 114 reflections, indicating all superlattices are coherently grown on STO substrates.

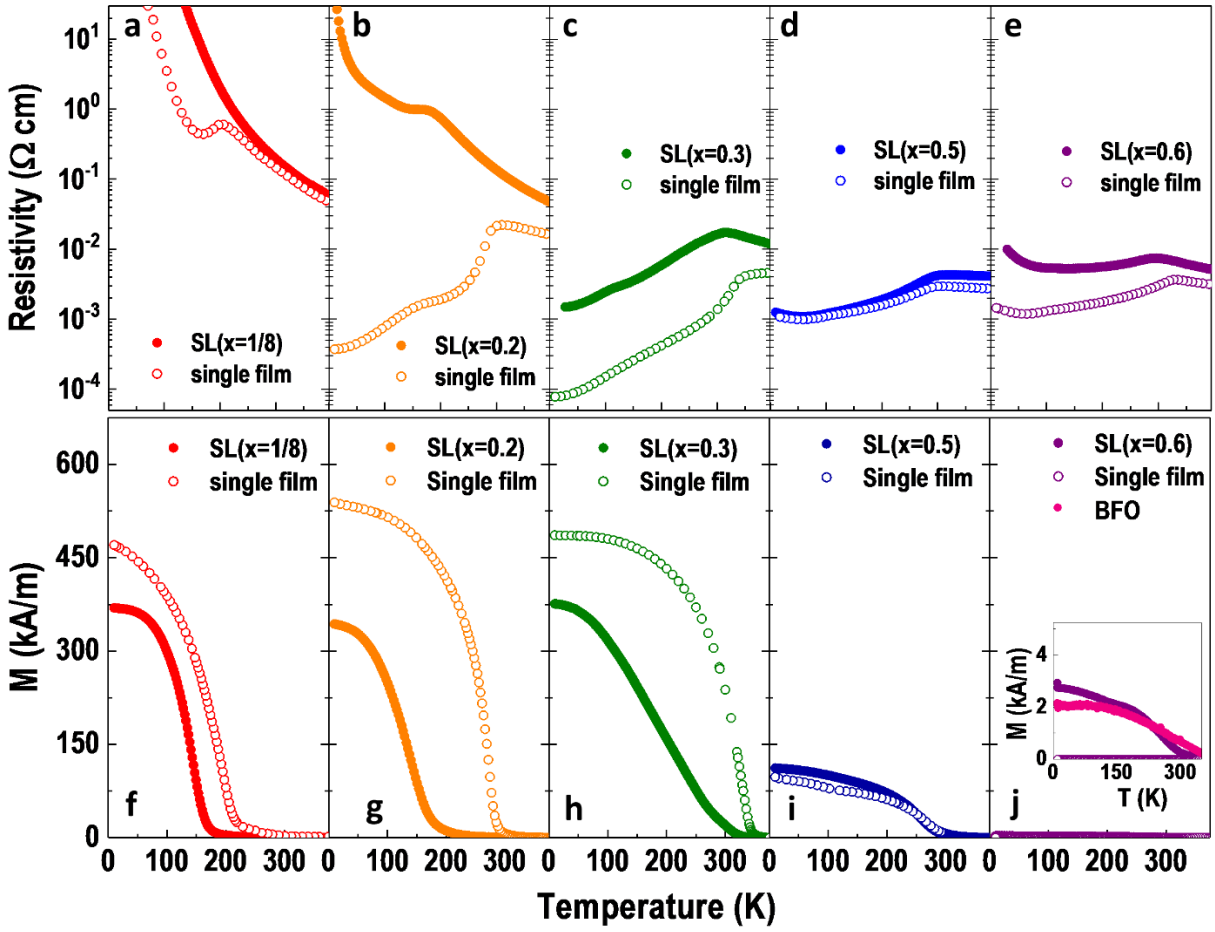

Figure 3. Transport properties of BFO/LSMO SLs and LSMO single layers. **a** to **e**. $R(T)$ curves and **f** to **j**. $M(T)$ curves of all (100)-SLs with various x. $R(T)$ and $M(T)$ curves of LSMO single layers and (100)-SLs with the same x are shown in the same plot for comparison. $R(T)$ measurements were conducted under zero magnetic field during the sample warming-up. $M(T)$ measurements were performed under an in-plane magnetic field of 1 kOe. Inset of **j** shows the zoom-in illustration of $M(T)$ curves of a SL (x = 0.6) and a BFO single layer. The small magnetization from a SL (x = 0.6) is comparable to that of a BFO single layer at low temperatures, suggesting the magnetic response in SL (x = 0.6) comes from the BFO layers.

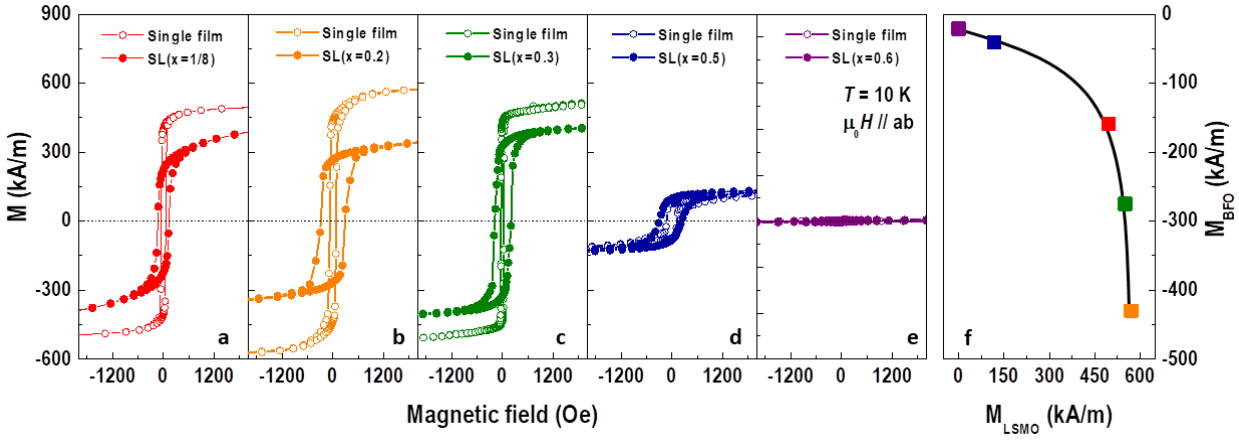

Figure 4. Magnetic hysteresis loops of BFO/LSMO SLs and LSMO single layers. **a-e**. *M*(*H*) loops of LSMO single layers and SLs with the same *x* are shown in the same plot for comparison. *M*(*H*) loops were measured at 10 K after field cooling in 1 kOe. The magnetic field was applied along the in-plane direction. **f**. The induced magnetization in BFO layers as a function of the saturation magnetization of LSMO layers. The magnetization of BFO layer is antiparallel to that of the LSMO layer due to the antiferromagnetic exchange coupling.

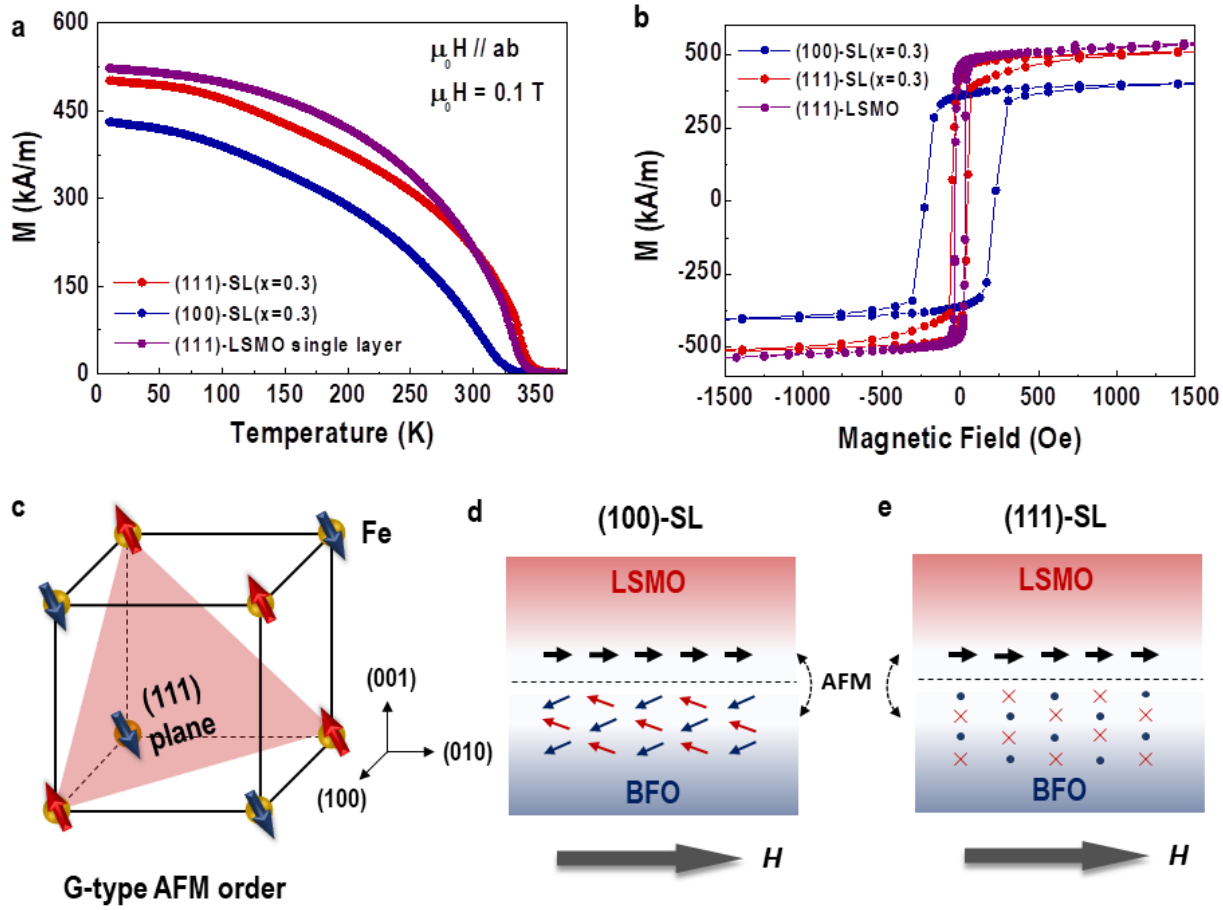

Figure 5. Magnetic properties of BFO/LSMO SLs with different crystallographic orientations. **a**. *M*(*T*) curves and **b**. *M*(*H*) loops of a (111)-LSMO single layer, a (111)-SL, and a (100)-SL, respectively. *M*(*T*) curves were measured after field cooling in 1 kOe. *M*(*H*) loops were recorded at 10 K with applied in-plane magnetic field. **c**. Schematic of G-type AFM spin ordering in bulk BFO. **d** and **e**. Schematic of spin alignments across the (100)- and (111)-oriented BFO/LSMO interfaces, respectively. The spins from Fe and Mn ions are AFM coupled across the interfaces. In (111)-SL, the spins of Fe ions cant along the field direction due to the Dyzaloshinskii–Moriya Interaction (DMI), producing a small net moment. This behavior is the same with the bulk BFO.

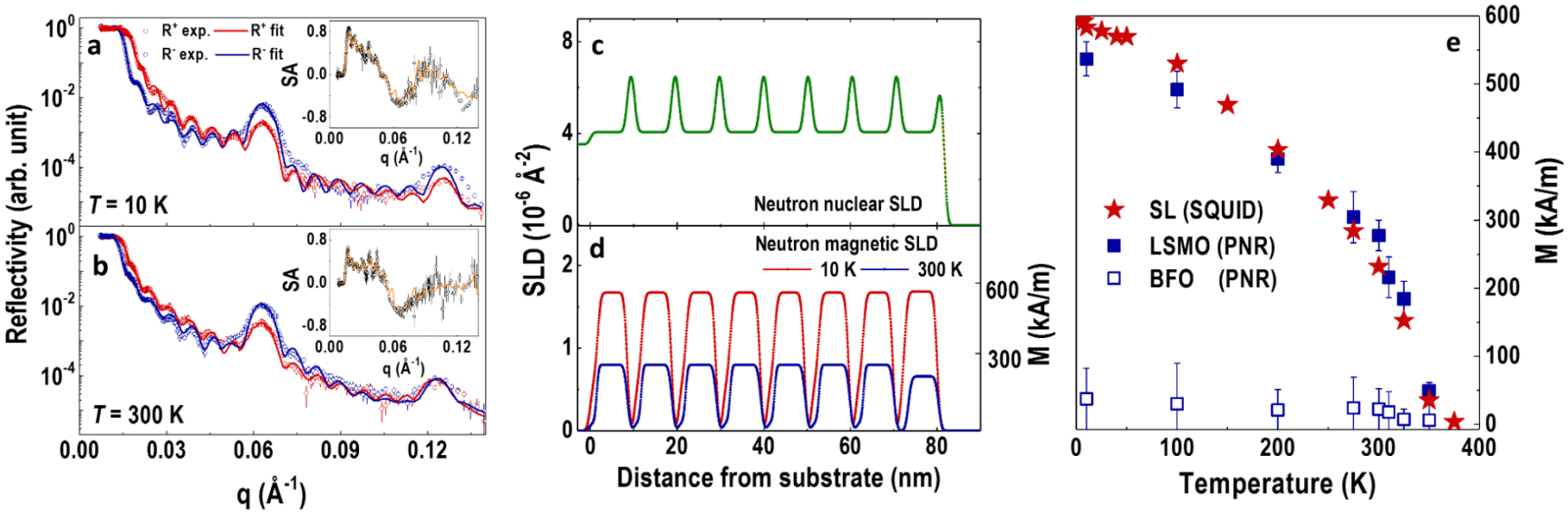

Figure 6. Polarized Neutron Reflectometry (PNR) measurements on a (111)-oriented BFO/LSMO SL. Measured (open symbols) and fitted (solid lines) reflectivity curves for spin-up (R^+) and spin-down (R^-) polarized neutrons are shown as a function of wave vector q. **a** and **b** show the PNR results measured at 10 and 300 K, respectively. PNR measurements were performed after field cooling in 1 T. The insets of **a** and **b** show the spin asymmetries (SA) of corresponding PNR data and fits. **c** and **d**. Depth profiles of neutron nuclear and magnetic scattering length densities (SLD), respectively. **e**. PNR-derived magnetization of BFO (blue open squares) and LSMO (blue solid squares) layers as a function of temperature. The saturation magnetization of the same (111)-SL measured from SQUID (red stars) is shown for comparison.